ROYAL SOCIETY
OF CHEMISTRY

PAPER

Check for updates

Modulation of supported Ni catalysts with phosphorus for the hydrogenation of diethyl oxalate to ethyl glycolate†

Qihong Xue,[ab] Zhikui Jiang,[c] Chao Wang,[ab] Xian Kan,[ab] Jiaming Wang[a] and Jiangang Chen ✶[a]

In this study, 13-Ni/ZrO$_2$, 13-Ni$_3$P/ZrO$_2$, 13-Ni/SiO$_2$, and 13-Ni$_3$P/SiO$_2$ catalysts were used in the hydrogenation of diethyl oxalate (DEO) to ethyl glycolate (Egly) to investigate the modulating effect of phosphorus. XRD, TEM, and FT-IR spectroscopy results indicated that phosphorus acts as a distributor of Ni metallic particles and thereby shows a segregation effect. The presence of P transformed the linkage of surface metals from an original Ni–Ni–Ni–Ni– to a P–Ni–P–Ni–P state, and FT-IR spectra showed that the former adsorbed CO in a combination of linear and bridging adsorption modes, whereas the latter predominantly in CO linear adsorption. Bridging adsorption occurs *via* dual sites and makes preliminary hydrogenation products less likely to detach from the catalyst surface, thus facilitating deep hydrogenation, while linear adsorption facilitates partial hydrogenation *via* rapid detachment of intermediate products such as Egly. Different loadings of Ni$_3$P/SiO$_2$ catalysts show incomplete phosphorylation with an increase in nickel loading, giving rise to a state of coexistence of Ni and Ni$_3$P crystalline phases. This may lead to a coexistence of surface Ni–Ni–Ni–Ni and P–Ni–P–Ni–P and an increase in the corresponding bridging adsorption/linear adsorption ratios, making deep hydrogenation occur partially besides stepwise hydrogenation.
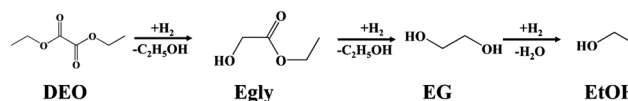
1. Introduction

Ethyl glycolate (Egly) is a kind of fine chemicals with considerable academic and commercial benefits. Owing to its unique molecular structure with α-H, hydroxyl, and ester groups, Egly can undergo carbonylation, oxidation, and hydrolysis.[1] As a raw material, it is widely used in the synthesis of pharmaceuticals, fine chemicals, and perfumes. Recently, polyglycolic acid (PGA) as degradable plastic has attracted much attention.[2] It has been reported that PGA not only has great significance for ecological health, owing to its excellent biocompatibility and biodegradability, but also has a large market potential owing to the independent supply of starch, whose scarcity restricted its wide application as degradable plastic feedstock.[3] Therefore, the task of producing glycolate in an efficient and environment-friendly manner has become particularly urgent nowadays.

There are many ways such as the carboxylation of formaldehyde[4] and coupling of formaldehyde and methyl formate[4b] to produce glycolate, but these approaches are limited by harsh production conditions and low yields.[5] However, the unique advantages of the "C1 chemical route", namely, a wide range of products from feedstock sources (such as coal, natural gas, renewable biomass, and organic waste) to syngas exhibiting high yields, environmental friendliness, and atomic economy, offer us a new alternative route.[6] Palladium-catalyzed CO coupling with nitrite for the synthesis of oxalate and the partial hydrogenation of oxalate to glycolate is considered to be the most promising route.[3a,7] Oxalate hydrogenation is a successive reaction; typically, oxalate is initially hydrogenated to form glycolate, followed by further hydrogenation to ethylene glycol (EG), and finally EG hydrolysis to ethanol (EtOH) (Scheme 1).[8] The thermodynamic constant of glycolate to EG is two orders of magnitude, which is larger than that of oxalate to glycolate.[9] There is no doubt that achieving high selectivity in the

[a] *State Key Laboratory of Coal Conversion, Institute of Coal Chemistry, Chinese Academy of Sciences, Taiyuan 030001, Shanxi, P. R. China. E-mail: chenjg@sxicc.ac.cn*

[b] *University of Chinese Academy of Sciences, Beijing 100049, P. R. China*

[c] *China Shenhua Coal to Liquid Chemical Co., Ltd, China*

† Electronic supplementary information (ESI) available. See DOI: https://doi.org/10.1039/d3nj05483g

Scheme 1 DEO gas-phase hydrogenation pathways.

initial hydrogenation of oxalate to a target product is challenging, and the most critical issue in this regard is the development of efficient, stable, and low-cost catalysts.

Catalysts for the initial hydrogenation of oxalate to glycolate are broadly classified into two main categories: homogeneous and heterogeneous. Among them, Ru-based catalysts are the typical representatives of homogeneous catalysts. Boardman *et al.*[10] designed a catalyst utilizing a sulfur-based ligand [MeC(CH$_2$SBu)$_3$] for the selective hydrogenation of dimethyl oxalate (DMO) to methyl glycolate (MG), which shows 100% MG selectivity in a 136 h test. However, the high cost of ruthenium metal, the difficulty in separating the by-products, and the harsh reaction conditions have limited its commercialization. As far as we know, current research on heterogeneous catalysts for the initial hydrogenation of oxalate to MG has mostly focused on Cu- or Ag-based catalysts. The Cu-based catalysts were prepared in a simple way and several supports including activated carbon (AC),[11] reduced graphene oxide (RGO),[12] hydroxyapatite (HAP),[13] ZrO$_2$–SiO$_2$,[14] SBA-15,[15] Ni-foams,[16] and MgO[17] were employed to achieve high activity and stability. For instance, our research group reported that 25 wt% Cu/RGO catalyst exhibited remarkable performance, with 100% DMO conversion and 98.8% selectivity of MG in a duration of 300 h at 210 °C.[12] However, Cu-based catalysts suffer from the complex challenges of precise Cu^0/Cu$^+$ site regulation, poor stability, irreconcilable conversion and glycolate selectivity,[3a,18] which still need to be further addressed. Ag-based catalysts have attracted much attention from researchers due to their relatively poor hydrogenation ability and relatively high MG selectivity in oxalate-to-glycolate processes compared to Cu-based catalysts. Chen *et al.*[8] have found that the relatively weak Ag–SiO$_2$ interaction makes Ag/SiO$_2$ especially vulnerable to deactivation and poor stability, and doping with B$_2$O$_3$ can improve this condition. Nevertheless, Ag-based catalysts are limited in scale and practical application due to their precious metal properties and low activity.

Nickel phosphide catalysts exhibit properties like noble metals, showing unique physical properties such as high strength and hardness as well as high activity and stability in hydrogenated environments. They have attracted great attention and have been successfully applied to electrocatalysis, photocatalysis, and thermocatalysis.[5,19] Recently, Chen *et al.*[20] have found that Ni$_2$P/TiO$_2$ catalysts can provide 100% conversion of DMO and 76% selectivity to MG during the 3600 h time-on-stream under the reaction conditions of 230 °C, 3 MPa H$_2$ and the weight space velocity (WHSV) of 0.1 h^{-1}, achieving the first breakthrough of nickel phosphide in the hydrogenation of DMO to MG reaction. Furthermore, Zhu *et al.*[6a] reported that a Ni$_3$P/Ni-foam catalyst can achieve almost full DMO conversion with a high MG selectivity of 95–97% and is stable for at least 1000 h without any sign of deactivation at 230 °C, 2.5 MPa and a WHSV of 0.44 h^{-1}. Using density functional theory (DFT), they found that Ni$_3$P has a higher electron density, which is favorable for MG adsorption in the molecular structure and suppresses the deep hydrogenation of MG to EG. Meanwhile, Zhao *et al.*[3a] reported that a Ni$_3$P/RB-MSN catalyst is capable of

fully converting DMO with 85.0% MG selectivity and stable for at least 500 h at 190 °C. The lack of Si–OH in RB-MSN diminishes the interaction of NiO and PO$_x$ with Si–OH groups, which favors the formation of Ni$_3$P and suppresses the formation of harmful irreducible PO$_x$ species.

The previous studies made efforts to explain the outstanding effect of the electron density of Ni$_3$P itself and investigate the role of the corresponding *meso*-SiO$_2$ supports on the reaction performance. SiO$_2$ is usually regarded as an inert support, whereas ZrO$_2$ is functional due to its rich O vacancy. However, the effect of phosphorylation on the form of adsorption of substrate molecules (linear or bridging adsorption) and the role of P in Ni$_3$P formed by phosphorylation (anti-agglomeration and segregation effects) during the nickel phosphide-catalyzed hydrogenation of diethyl oxalate (DEO) to Egly compared to pure Ni are not reported. In this work, we prepared 13-Ni/ZrO$_2$, 13-Ni$_3$P/ZrO$_2$ and 13-Ni/SiO$_2$ (13 is the weight percentage of Ni), and *X*-Ni$_3$P/SiO$_2$ (*X* represents the weight percentage of Ni: 6, 13, and 25, respectively) by an incipient wetness impregnation method and the subsequent hydrogen temperature-programmed reduction treatment. We found that both 13-Ni$_3$P/SiO$_2$ and 13-Ni/SiO$_2$ catalysts achieved full conversion of DEO under identical reaction conditions, but the selectivity for Egly (55% *vs.* 32%), EtOH (40% *vs.* 62%), and EG (2.7% *vs.* 4.4%) differed dramatically. In addition, the 6,13,25-Ni$_3$P/SiO$_2$ catalyst gradually showed a deep hydrogenation performance inclined to that of the 13-Ni/SiO$_2$ catalyst by decreasing the selectivity of Egly from 60% to 51% and increasing the selectivity of EG from 1% to 4% with the increase in metal loading. Compared with the 93% conversion of the 13-Ni$_3$P/ZrO$_2$ catalyst, the conversion of the 13-Ni/ZrO$_2$ catalyst was only about 60% with a tendency of gradual deactivation. To elucidate the underlying physicochemical properties and surface adsorption mechanism and gain deep insights into the actual reaction process, we performed *in situ* DRIFT-IR spectroscopy using CO as a probe molecule in combination with XRD, XPS, TEM, H$_2$-TPR, and N$_2$ adsorption/desorption isotherm characterization.

2. Experimental

2.1. Catalyst preparation

The Ni$_3$P catalyst was synthesized *via* the traditional temperature-programmed reduction method as previously reported with slight modifications.[21] Silica-supported Ni$_3$P catalysts were prepared by incipient wetness impregnation using nickel nitrate (Ni(NO$_3$)$_2$·6H$_2$O – Sinopharm Chemical Reagent Co., Ltd, analytical reagent (AR)) as the nickel precursor and ammonium hydrogen phosphate ((NH$_4$)$_2$HPO$_4$ – Tianjin Wind Ship Chemical Reagent Technology Co., Ltd, AR) as the phosphorus precursor. Taking Ni$_3$P/SiO$_2$ as an example, first, under vigorous stirring, Ni(NO$_3$)$_2$·6H$_2$O (5.81 g) and (NH$_4$)$_2$HPO$_4$ (0.88 g) were added to 20 ml of deionized water with a Ni/P molar ratio of 3. Next, an appropriate amount of HNO$_3$ solution (65 wt%) was added to adjust the pH to 2–3 to obtain a clear solution,

and the solution was used to impregnate silica (SiO$_2$ – MACKLIN, S_{BET} = 400 m^2 g^{-1}) by the incipient wetness method. After aging at room temperature for 12 h, the obtained samples were dried at 110 °C for 12 h and calcined in air at 500 °C for 4 h. The precursor particles were reduced to nickel phosphide under an H$_2$ stream (80 ml min^{-1}) as the temperature was increased from room temperature to 400 °C at a ramp of 5 °C min^{-1} and held at 400 °C for 1 h, followed by an increase from 400 °C to 650 °C at a ramp of 2 °C min^{-1} and held at 650 °C for 2 h. After reduction, the Ni$_3$P/SiO$_2$ catalyst (Ni loading of 13 wt%) was cooled to room temperature under an Ar stream and was passivated under a 1% O$_2$/99%N$_2$ stream for 2 h. A series of catalysts including 13-Ni/ZrO$_2$ (ZrO$_2$-aladdin) and 13-Ni/SiO$_2$ (phosphorus-free, Ni loading of 13 wt%), 13-Ni$_3$P/ZrO$_2$ (Ni loading of 13 wt%), and 6,13,25-Ni$_3$P/SiO$_2$ were also prepared and reduced using the same procedures as described above.

2.2. Catalyst characterization

X-ray diffraction (XRD) measurement was conducted to analyze the structure and crystallinity of the active phase of nickel phosphide. XRD patterns were obtained using a Shimadzu XRD-6000 diffractometer with Cu Kα radiation (λ = 1.5418 Å) in the 2θ range from 5° to 80° at a scanning rate of 4° min^{-1}.

Transmission electron microscopic (TEM) and high-resolution TEM (HRTEM) images were acquired using a JEM 2100F. Before imaging, the catalyst sample was ultra-sonically dispersed in ethanol and dropped onto a carbon-coated copper grid. Meanwhile, the elemental compositions of the catalysts were identified by an EDS mapping analysis.

The specific surface areas (S_{BET}) were determined through Brunauer–Emmett–Teller (BET) measurements using a Tristar II3020 N$_2$ adsorption analyzer. In addition, the average pore diameters and pore size distributions were analyzed by the Barrett–Joyner–Halenda (BJH) method.

X-ray photoelectron spectroscopy (XPS) measurements were carried out using a Thermo Scientific ESCALAB 250Xi to determine the surface composition and valence state of the elements. The binding energies (BEs) were calibrated referencing adventitious C 1s at 284.8 eV. The actual P and Ni loadings of catalysts were quantitatively determined by inductively coupled plasma-atomic emission spectroscopy (ICP-AES) using a 730/Agilent 7700.

H$_2$-temperature-programmed reduction (H$_2$-TPR) profiles of the catalyst precursors were obtained in a laboratory-built programmed-temperature reduction installation constructed with a gas chromatograph (GC-950) and an energy-efficient tubular resistance furnace (SKZ-25-BD), as well as a computer for data recording. First, 100 mg of catalyst was heated at a flow rate of 50 ml min^{-1} (H$_2$/N$_2$ = 5%) to 800 °C at a rate of 10° min^{-1}. H$_2$ consumption was recorded during this ramp-up process using a thermal conductivity detector (TCD).

For NH$_3$-TPD, each sample of 0.1 g was first reduced in a temperature-programmed way under a 5 vol% H$_2$/Ar flow (30 ml min^{-1}) from 50 to 500 °C at a heating rate of 10 °C min^{-1} to remove the passivated layer, and after cooling down to 50 °C under a Ar flow (30 ml min^{-1}), the sample was continuously treated under a 5

vol% NH$_3$/Ar flow (30 ml min^{-1}) at 50 °C for 0.5 h to fully adsorb NH$_3$ followed by 30 min Ar purging at room temperature, and finally, the sample was heated from 50 to 600 °C under an Ar flow at a rate of 30 ml min^{-1} at a heating rate of 10 °C min^{-1}.

In situ time-resolved diffuse reflectance Fourier transform infrared (DRIFT-IR) spectroscopy of CO adsorption was performed using a Bruker TENSOR27 FT-IR spectrometer equipped with an MCT detector. For CO adsorption, the sample in the cell was pre-treated at 450 °C for 1 h under a pure H$_2$ flow (30 ml min^{-1}) to remove the passivated layer and then cooled to 220 °C (simulation of actual reactant temperature) under an Ar flow, and the background spectrum was recorded at this time. Then, a 10% CO/90% N$_2$ flow was introduced into the cell at a rate of 30 ml min^{-1} for 30 min. Finally, an Ar flow (30 ml min^{-1}) was switched to remove the free CO molecules, and the spectrum of 1000–4000 cm^{-1} was recorded at 1, 5, 10, 15, 25, 35, 45, and 55 min.

2.3. Catalytic test

DEO gas-phase hydrogenation performance testing of nickel phosphide catalysts was performed using a fixed-bed reactor. The nickel phosphide catalyst was tested under the following conditions: T = 190–230 °C, WHSV = 1–2 h^{-1}, H$_2$/DEO = 40, 80, and 120, and P = 1.5, 2, and 2.5 MPa. A mass of 0.6 g of X-Ni$_3$P/SiO$_2$ or 1.0 g of 13-Ni$_3$P/ZrO$_2$ catalyst was placed in a 10 mm-diameter stainless steel reaction tube. The nickel phosphide catalyst was placed in the thermostatic zone of the reactor and the upper and lower ends were filled with quartz sand. Before the reaction starts, the nickel phosphide catalyst is reduced again to remove the passivated layer at 500 °C in a fixed bed under an H$_2$ atmosphere of 80 ml min^{-1} for 2 h. DEO is pumped from the feedstock tank into the fixed bed reactor using a double plunger pump. A gasification unit with a temperature of 200 °C is installed between the pump outlet and the fixed bed reactor inlet. The analysis of the liquid phase products was performed using a gas chromatograph equipped with a capillary column (Agilent HP-INNOWAX) and an FID detector. The detection of small amounts of water in the samples was performed using a chromatograph equipped with a TCD detector and a TDX-101 column. DEO conversion and product selectivity were calculated as follows [eqn (1) and (2)]:

$$\text{DEO conversion} = \left(1 - \frac{\text{Moles of unreacted DEO}}{\text{Moles of DEO in the feed}}\right) \times 100\%$$

(1)

$$\text{Product selectivity} = \frac{\text{Moles of a product}}{\text{Moles of all liquid products}} \times 100\%$$

(2)

3. Results

3.1 Characterization of the catalysts

Physicochemical properties of the catalysts. The textual information of the as-prepared catalysts is summarized in Table 1.

Table 1 Physicochemical properties of 13-Ni/ZrO$_2$, 13-Ni$_3$P/ZrO$_2$, 13-Ni/SiO$_2$, and 6,13,25-Ni$_3$P/SiO$_2$ catalysts

| Catalyst | S_{BET}^a (m^2 g^{-1}) | V_{pore}^b (cm^3 g^{-1}) | D_{pore}^c (nm) | Content^d (wt%) | | Bulk Ni/P^d | Surficial Ni/P^e | Crystal size^f (nm) |
				Ni	P			
13-Ni/ZrO$_2$	8	0.04	19.45	12.08	—	—	—	56.40
13-Ni$_3$P/ZrO$_2$	11	0.06	20.00	11.96	1.24	5.09	18.72	9.50
13-Ni/SiO$_2$	262	0.71	10.56	12.92	—	—	—	27.30
6-Ni$_3$P/SiO$_2$	274	0.79	11.24	6.06	1.04	3.08	8.24	1.14
13-Ni$_3$P/SiO$_2$	240	0.70	11.19	12.56	2.17	3.05	4.37	15.30
25-Ni$_3$P/SiO$_2$	208	0.61	11.27	23.19	4.06	3.01	4.40	20.90
ZrO$_2$	8	0.03	14.40	—	—	—	—	—
SiO$_2$	400	—	—	—	—	—	—	—

^{a} Specific surface area determined using the standard Brunauer–Emmett–Teller theory on the N$_2$ adsorption isotherm. ^{b} Pore volume estimated from the amount of N$_2$ adsorbed at P/P_0 = 0.99. ^{c} Pore diameter determined using the Barrett–Joyner–Halenda (BJH) theoretical model. ^{d} Measured *via* ICP-OES analysis. ^{e} Measured *via* XPS analysis. ^{f} Calculated using the Scherrer equation from XRD patterns.

The ICP-AES results indicate that the measured values of the Ni/P molar ratio in the synthesis catalyst are consistent with the theoretical values. However, the surface Ni/P molecular ratio values obtained by XPS are all significantly higher than the bulk phase values measured by ICP. This may be due to the fact that some of the P escapes as phosphine gas during the high-temperature reduction process and others present as phosphide that is more stabilized in the bulk phase. With the increase in nickel content, from 6, 13 to 25-Ni$_3$P/SiO$_2$ catalyst, S_{BET} and V_p decreased. This may be due to the increase in particle size and incomplete phosphorylation. Naturally, ZrO$_2$ is a low surface support, while the values of S_{BET}, V_p, and D_p for 13-Ni/ZrO$_2$ and 13-Ni$_3$P/ZrO$_2$ catalysts were greater than or equal to that of ZrO$_2$. This may be caused by the small specific surface area of the carrier itself, and the active substances might form additional pore structures.

Morphology and crystalline phase of the catalysts. X-ray diffraction (XRD) patterns were used to identify the crystalline phases formed after reduction. Fig. 1A gives the XRD patterns of 13-Ni/ZrO$_2$ and 13-Ni$_3$P/ZrO$_2$ samples. Both catalysts exhibited strong diffraction peaks for the ZrO$_2$ (PDF#37-1484) carrier, since it was a well-crystalized material. The diffraction peaks for the Ni phase are relatively weak. The 13-Ni$_3$P/ZrO$_2$ catalyst shows diffraction peaks at 2θ values of 41.76, 43.63, 45.21, and 46.61°, which are assigned to the (231), (112), (240), and (141) lattice planes of the Ni$_3$P crystallites (PDF#34-0501).

However, compared to the 13-Ni$_3$P/ZrO$_2$ catalyst, the spectra of the 13-Ni/ZrO$_2$ catalyst showed relatively stronger diffraction peaks at 2θ = 44.51, 51.85 and 76.37° corresponding to the Ni crystalline phase. This phenomenon suggests that phosphatization makes contribution to reducing the particle size of nickel and enhancing the dispersion of the nickel phosphide after phosphatization. As shown in Fig. 1B, the 13-Ni/SiO$_2$ and 13-Ni$_3$P/SiO$_2$ catalysts showed very similar phenomena, that is, the Ni species diffraction peaks became weaker after phosphorization. The intensity of the diffraction peaks of Ni$_3$P and Ni in the X-Ni$_3$P/SiO$_2$ catalysts increased gradually as the metal nickel loading was increased from 6, 13, to 25. For the 6-Ni$_3$P/SiO$_2$ catalyst, the intensity of Ni$_3$P diffraction peaks was rather weak and no Ni diffraction peaks were observed. As the metal loading increased, the intensity of Ni$_3$P diffraction peaks for 13-Ni$_3$P/SiO$_2$ and 25-Ni$_3$P/SiO$_2$ catalysts became stronger stepwise, Ni diffraction peaks started to appear in both of them, and the intensity of Ni diffraction peaks for 25-Ni$_3$P/SiO$_2$ catalyst was relatively strong. At the maximum loading, metallic Ni diffraction became apparent besides the peaks of the nickel phosphide. In other words, the coexistence of Ni$_3$P crystals and Ni crystals appeared in the highly loaded X-Ni$_3$P/SiO$_2$ catalysts. The Ni or Ni$_3$P crystal size was calculated from XRD. It can be seen clearly that phosphorylation is not complete if the Ni crystallite size is larger, while phosphorylation is more complete when the Ni crystallite is small. This pattern proves that
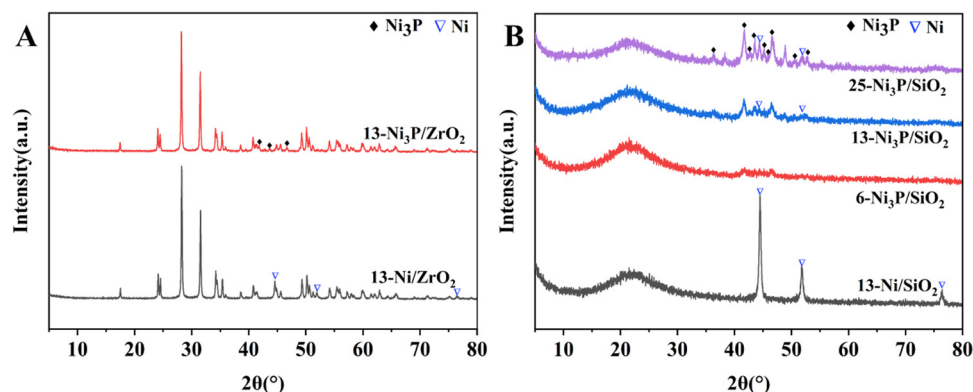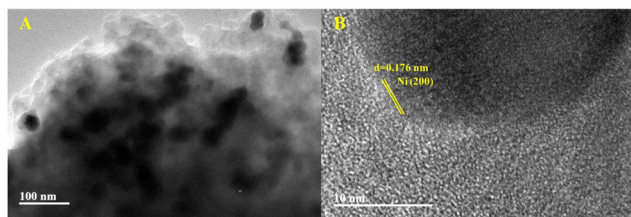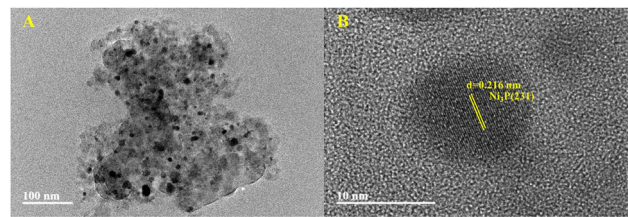

Fig. 1 XRD patterns of the synthesized catalysts.

Fig. 2 . TEM images of 13-Ni/SiO$_2$.

Fig. 4 TEM images of 13-Ni$_3$P/SiO$_2$.

Fig. 5 TEM images of 25-Ni$_3$P/SiO$_2$.

the Ni$_3$P yield depends on the Ni crystallite size in the precursor.

Ni$_3$P diffraction peaks for 13-Ni$_3$P/SiO$_2$ and 25-Ni$_3$P/SiO$_2$ catalysts were stepwise stronger and Ni diffraction peaks started to appear in both of them, and the intensity of Ni diffraction peaks for 25-Ni$_3$P/SiO$_2$ catalyst was relatively strong. This pattern proves once again that phosphorus in Ni$_3$P acts as a disrupter and shows a segregation effect, but it is clear that this effect (phosphorylation) is weakened with the increase in Ni loading and particle size.

As shown in Fig. 2–5B, the HRTEM images confirmed the formation of Ni crystalline phases in Ni/SiO$_2$ and Ni/ZrO$_2$ (Fig. S1B, ESI†) catalysts and Ni$_3$P crystalline phases in 13-Ni$_3$P/ZrO$_2$ (Fig. S2B, ESI†) and 6,13,25-Ni$_3$P/SiO$_2$ catalysts. The HRTEM images revealed that Ni particles with a lattice spacing of 0.176 nm are attributed to the (200) plane, while Ni$_3$P particles with a lattice spacing of 0.216 nm are attributed to the (231) plane, and in particular Ni$_3$P particles with a lattice spacing of 0.197 nm are attributed to the (202) plane as probed in the 25-Ni$_3$P/SiO$_2$ catalyst. Furthermore, the EDS mapping of Fig. 6A and B shows that Ni and P are homogeneously dispersed in the catalyst. This can also be verified from Table 1 crystal size calculations, where the average grain size is 56.4 nm for the 13-Ni/ZrO$_2$ catalyst and decreased to 9.50 nm for the 13-Ni$_3$P/ZrO$_2$ catalyst. Similarly, the dimension is 27.30 nm for the 13-Ni/SiO$_2$ catalyst and decreased to 15.30 nm for the 13-Ni$_3$P/SiO$_2$ catalyst. Meanwhile, with the increase in Ni loading of 6,13, 25-Ni$_3$P/SiO$_2$ catalysts, the grain size also increased sequentially (1.14, 15.30, and 20.90 nm), which was not favorable for phosphatization.

Reducibility properties. In order to investigate the interaction between active species and carriers and compare the reduction behavior of catalysts during phosphorization, various nickel contents and different supports are tested in H$_2$-TPR. As shown in Fig. 7, both 13-Ni/SiO$_2$ and 13-Ni/ZrO$_2$ catalysts have a major peak around 400 °C, which is attributed to the reduction

Fig. 3 TEM images of 6-Ni$_3$P/SiO$_2$.

of bulk phase nickel oxide to nickel metal, whereas 13-Ni/ZrO$_2$ catalysts show a double peak, which may be due to the different sizes of nickel oxide particles. The tail peak at higher temperatures may be formed by nickel silicate. This pattern is in agreement with the findings of other researchers.[22] With the P-containing precursor, 6,13,25-Ni$_3$P/SiO$_2$ catalyst, the reduction temperature of nickel oxide was gradually shifted to higher temperatures at 415 °C. The more the Ni loading, the higher the temperature peak, which may be due to the larger particle size. It is noteworthy that the double peak at 400 °C for the 6-Ni$_3$P/SiO$_2$ catalyst might also be due to the inhomogeneous particle size. Compared to pure Ni, the H$_2$-TPR profile of the catalyst with phosphatization is more complex, in which the TPR peak at 700 °C is attributed to the formation of nickel phosphate between Ni and PH$_3$, which has to be formed at 700 °C due to the high thermodynamic stability of the P–O bond.[22a] Meanwhile, Liu *et al.* found that the reduction temperature of nickel phosphate for nickel phosphide catalysts with a lower phosphorus content was lower than that of those with a higher phosphorus content, which could be due to the function of metallic nickel that adsorbs and dissociates hydrogen that can be spilled over into phosphates to promote the reduction of phosphates to generate phosphorus or hydrogen phosphide. Phosphorus or hydrogen phosphide can react with nickel particles to form nickel phosphide.[22a,23]

FT-IR study of CO adsorbed on catalysts. In the investigation of heterogenous catalyst surface, CO, a model molecule with the functional group of C=O, is widely used as a probe molecule in the *in situ* DRIFT-IR technique to investigate the chemisorption properties of nickel sites on the catalyst surface.[24] As shown in Fig. 8A and B, the time-resolved DRIFT-IR spectra for the 13-Ni/ZrO$_2$ and 13-Ni$_3$P/ZrO$_2$ catalysts disclosed two intense bands at *ca.* 2115 and 2170 cm^{-1}, due to the typical free or physisorbed CO molecules, which can be eliminated after 10 min with the purge of Ar flow.[24,25] In
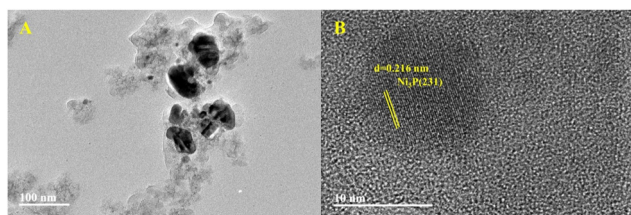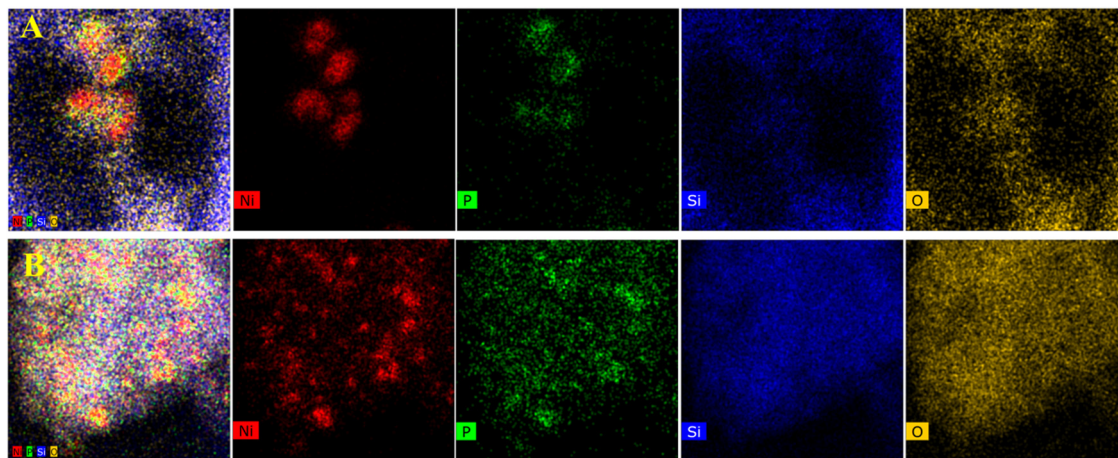
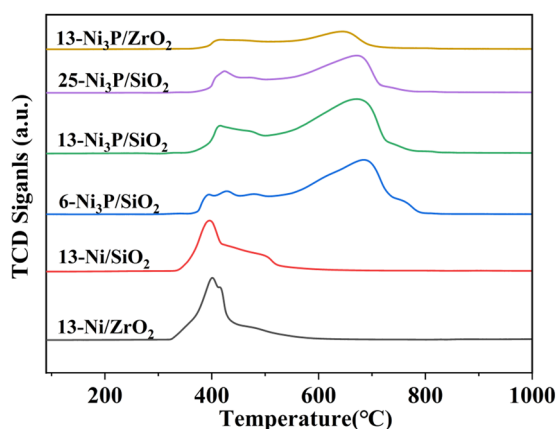**Fig. 6** EDS elemental mapping of (A) 6-Ni_3P/SiO_2 and (B) 13-Ni_3P/SiO_2.

Fig. 7 H_2-TPR profiles of catalyst precursors.

Fig. 8D, it is shown that the bands at *ca.* 2077 and 1800–1900 cm^{-1} are attributed to linear and bridged adsorption of CO molecules, respectively,[24,25] but the intensity gradually decreases upon Ar purging. After 55 minutes of purging, those peaks disappeared completely. It is a rather different story in the Ni_3P case, where an intense band can be detected at *ca.* 2077 cm^{-1} (linear adsorption), its extinction coefficient is large and the adsorption peak remains well after 55 min of Ar purge (Fig. 8E and F). Fig. 8C does not show any form of adsorption peaks for CO, which could be attributed to the lower loading of the 6-Ni_3P/SiO_2 catalyst with good dispersion and smaller particle size, and hence, weaker adsorption strength.

XPS. The superficial electron states of 13-Ni/ZrO_2 and 13-Ni/SiO_2 were investigated by means of XPS (Fig. 9). In the Ni $2p_{3/2}$ region, the peaks at 852.6–853.5, 855.4–856.3 and 861.1–861.92 eV were attributed to $Ni^{\delta+}$, oxidized Ni species, and satellite peak, respectively.[26] The ratio of $Ni^{\delta+}$ to oxidized Ni^{2+} in the XPS spectra for the 13-Ni/SiO_2 catalyst was higher than that for the 13-Ni/ZrO_2 catalyst, suggesting that surficial Ni of 13-Ni/SiO_2 catalysts was more resistant to air exposure than 13-Ni/ZrO_2 catalyst during the passivation and exposure to air.[27]

The XPS spectra of 13-Ni_3P/ZrO_2 and 6,13,25-Ni_3P/SiO_2 in the Ni $2p_{3/2}$ and P 2p regions are shown in Fig. 10. The peak at the binding energy (B.E.) of 852.5–853.0 eV is attributed to $Ni^{\delta+}$, possibly in the form of Ni_3P due to partial electron transfer from Ni to P.[28] Compared with 13-Ni/ZrO_2, the $Ni^{\delta+}$ composition became larger in 13-Ni_3P/ZrO_2, suggesting phosphating aid to stabilize the low-valency Ni during passivation. The peaks of oxidized species at B.E.s of 855.9–856.6 eV for Ni^{2+} and 133.4 eV for P oxide might be associated with the surface oxidation of nickel phosphide in the passivation and subsequent exposure to air.[29] Interestingly, the ratio of metallic $Ni^{\delta+}$ to oxidized Ni^{2+} in the XPS spectra gradually decreases with the increase in nickel loading of the 6,13,25-Ni_3P/SiO_2 catalyst. This may be associated with the increased size of nickel particles and less phosphatization, leading to a larger proportion of metallic nickel present in the catalyst.

In the region of P 2p, two peaks of P $2p_{3/2}$ and P $2p_{1/2}$ at 129.5 and 130.5 eV were assigned to partially negative $P^{\delta-}$ ($0 < \delta < 2$) in Ni_3P.[26a,d] For 6,13,25-Ni_3P/SiO_2, two peaks at 127.0–127.4 and 128.9–130.0 eV appeared, and both were lower than those of elemental phosphorus (130.2 eV). The two peaks are assigned to reduced $P^{\delta1-}$ and $P^{\delta2-}$ ($\delta1 > \delta2$).[27,30] Similarly, the total peak intensity of the two reduced P species was higher than that of the almost undetectable oxidized P species, suggesting that the Ni_3P catalyst was present at a more reduced state.[27] In other words, there is more nickel metal to provide electrons to phosphorus.

3.2. Catalytic performance of the catalysts

The catalytic performance of 13-Ni/ZrO_2, 13-Ni_3P/ZrO_2, 13-Ni/SiO_2, and 6,13,25-Ni_3P/ZrO_2 catalysts was tested in a continuous fixed-bed reactor using pure DEO raw materials, and the results are shown in Fig. 10. The 13-Ni/ZrO_2 catalyst achieved 72% DEO conversion at the beginning of the reaction, however, the conversion started to decrease rapidly with the increase in the running time and showed obvious signs of deactivation (Fig. 11A). In contrast, the 13-Ni_3P/ZrO_2 catalyst achieved 93% DEO conversion and about 56% Egly selectivity without any
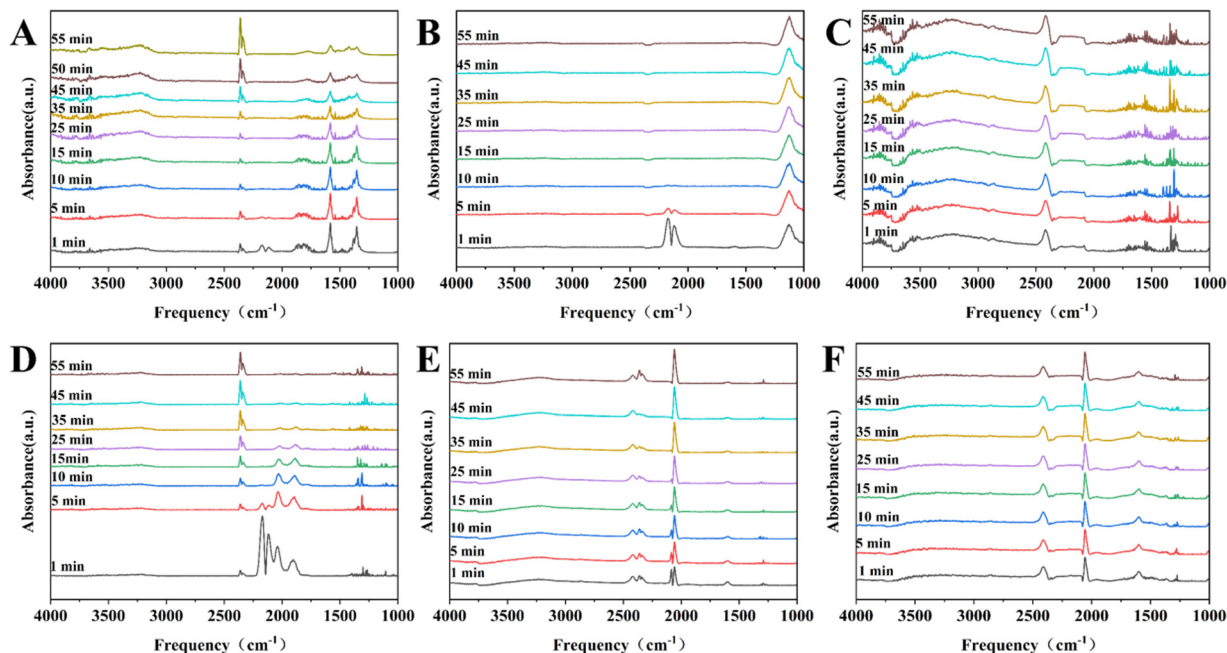
Fig. 8 Time-resolved DRIFT-IR spectra of CO adsorption for (A) 13-Ni/ZrO$_2$, (B) 13-Ni$_3$P/ZrO$_2$, (C) 6-Ni$_3$P/SiO$_2$, (D) 13-Ni/SiO$_2$, (E) 13-Ni$_3$P/SiO$_2$, and (F) 25-Ni$_3$P/SiO$_2$.

signs of deactivation over the run time (Fig. 11B). For comparison, between the above two catalysts, the latter catalyst showed a great improvement in stability after phosphorylation. Over 13-Ni/SiO$_2$, DEO conversion up to 99% was accompanied by a lower Egly selectivity of 31% and higher selectivities of 62% EtOH and 4.4% EG (Fig. 11D). Interestingly, the selectivities of Egly, EtOH, and EG were 55%, 40%, and 2.5%, respectively, over the 13-Ni$_3$P/SiO$_2$ catalyst at near-complete conversion of DEO (Fig. 11E). Compared with the catalytic performance of 13-Ni/SiO$_2$ catalysts, the 13-Ni$_3$P/SiO$_2$ catalysts exhibited a weaker ability for deep hydrogenation, or phosphorylation was favorable to inhibit the catalyst's ability for deep hydrogenation. Such a phenomenon is also observed in Ni/ZrO$_2$ systems. In addition, the catalysts on silica carriers (13-Ni/SiO$_2$, 13-Ni$_3$P/SiO$_2$) are more highly dispersed and show stronger metal–support interaction than those on zirconium dioxide carriers (13-Ni/ZrO$_2$ and 13-Ni$_3$P/ZrO$_2$) in terms of stability, activity, and selectivity.

As shown in Fig. 11C, E and F, the increase in the nickel loading of the 6,13,25-Ni$_3$P/SiO$_2$ catalyst had little effect on the conversion of DEO, which again verified the excellent performance of the Ni$_3$P active phase. The selectivity of Egly gradually decreased from 60% to 51%, which could be attributed to the combined effect of Ni and Ni$_3$P active phases. As the loading increased, it is performance similar to that of 13-Ni/SiO$_2$, showing more share of hydrogenation. This trend was more obvious for the EG selectivity, which increased from about 1% to about 4%.

Meanwhile, we also systematically investigated the effects of various reaction conditions on the performance of 13-Ni$_3$P/SiO$_2$ catalysts during the DEO hydrogenation reaction (see ESI†). The testing experiments were performed in the temperature range of 175–220 °C, WHSV range of 1.0–2.0 h^{-1}, H$_2$/DMO molar ratio range of 40–120, and pressure range of 1.5–2.5 MPa, with the results shown in Fig. S4 (ESI†). Remarkably, when the reaction temperature was decreased to 190 °C, 94% DEO conversion and 71% selectivity were still achieved for Egly. A further temperature drop to 185 °C (the boiling point of DEO is 185 °C) reduced the DEO conversion to 84%, and interestingly, at 175 °C, the catalyst still had 71% conversion (Fig. S4A, ESI†). The above performance demonstrates that the catalyst has a very wide operating window, which is important for the catalyst's large-scale application. In addition, the catalyst was more responsive to WHSV and H$_2$/DEO, but did not seem to be very sensitive to the changes in reaction pressure.

4. Discussion

4.1. Effect of phosphatization on the Ni surface texture

The role of phosphorus in nickel phosphide catalysts has been the subject of several studies. For example, Liu et al.[22b] suggested that the ensemble effect of P in nickel phosphide catalysts facilitates the decrease in the interaction between chlorine and nickel atoms, which promotes the hydrodechlorination reaction and the removal of chlorine ions from the catalyst surface. Similarly, Chen et al.[20] also suggested that the ensemble effect of P prevents the sintering of Ni$_2$P crystals and improves their stability at high temperatures. Cecilia et al.[31] showed that catalysts with high phosphorus amounts do not deactivate at high oxygen concentrations, which may be due to the fact that water preferentially interacts with excess phosphorus on the surface of the catalysts, thus preventing the nickel phosphide particles from oxidation.
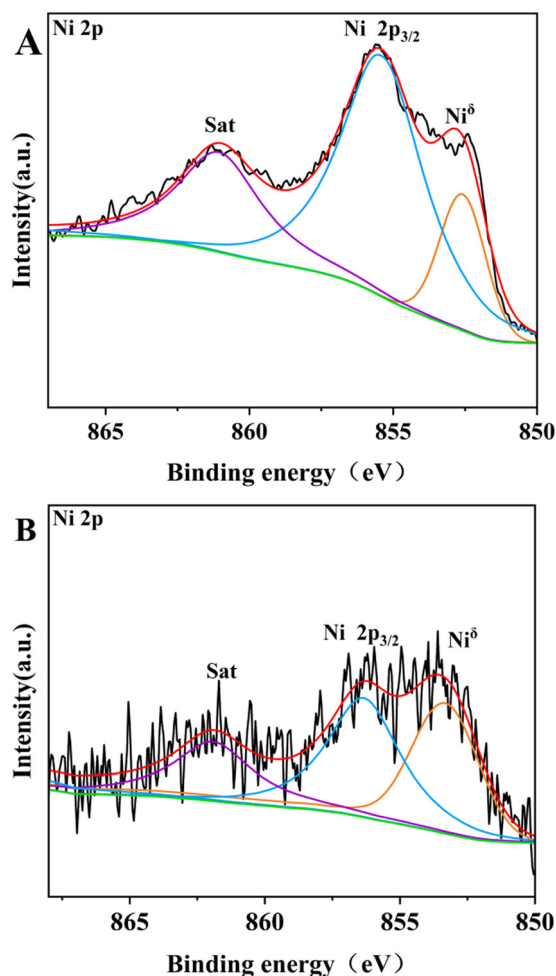
Fig. 9 XPS spectra of (A) 13-Ni/ZrO$_2$ and (B) 13-Ni/SiO$_2$ in Ni 2p regions.

In this work, for 13-Ni/ZrO$_2$ and 13-Ni$_3$P/ZrO$_2$ catalysts, the introduction of phosphorus favors an increase in the dispersion of the active substance and a decrease in crystallite size. This is verified by the calculations of the Scherrer equation, for instance, the decline in grain size from 56.4 nm for 13-Ni/ZrO$_2$ catalysts to 9.5 nm for 13-Ni$_3$P/ZrO$_2$ catalysts. This might explain the difference in stability and selectivity after phosphatization. This confirms the fact that the Ni$_3$P phase is a better catalytic phase than pure Ni. Meanwhile, the larger particle size may also be an important reason for the rapid sintering deactivation of 13-Ni/ZrO$_2$ catalysts. The large differences in the selectivity of Egly (31% *vs.* 55%), EtOH (62% *vs.* 40%), and EG (4.4% *vs.* 2.5%) for 13-Ni/SiO$_2$ and 13-Ni$_3$P/SiO$_2$ at both DEO conversions close to 99% illustrate the important role of P inhibiting hydrogenation from a deeper level. To trace the reasons, on the one hand, we argue that the emergence of P acts as a segregator and breaks the Ni–Ni linkage, demonstrating the anti-agglomeration effect, which has similar implications to the overall effect of P as suggested by previous researchers. The above conclusion can be verified from the XRD characterization results, and the diffraction peaks of Ni crystal phase are stronger than that of Ni$_3$P, indicating that the

grain size of single nickel is significantly larger than that of Ni$_3$P. Combined with the TEM characterization results, it can also be intuitively seen that the grain size of Fig. 2A is larger than that of Fig. 4A. In addition, the uniform distribution of nickel and phosphorus in the EDS mapping of Fig. 6B suggests that phosphorus may insert Ni$_3$P lattice evenly. The role of surface P atoms is both beneficial and detrimental, as argued by Bui *et al.*[19] The P atoms protect the stability of the nickel phosphide phase and destabilize the coke-producing Ni system. However, an excess of P atoms will overcover the exposed Ni sites and reduce the availability of active nickel sites. On the other hand, we suggest that Ni alone is prone to the surface metal structure of –Ni–Ni–Ni–Ni–, which is favorable for synergistic adsorption, *i.e.*, the co-existence of linear and bridging adsorption. The presence of P makes the surface texture shift from –Ni–Ni–Ni–Ni– to P–Ni–P–Ni–P mode, and the surface atom assembly in the latter is favorable for linear adsorption (Fig. 12). Therefore, it is proposed that the diversity of the adsorption form comes from surface atom arrangement after phosphatization. Such a texture change dominates the reaction performance, with phosphide displaying partial hydrogenation ability and yielding a higher Egly selectivity than that of pure Ni.

4.2. Effect of phosphatization on chemical adsorption and reactivity

The form of substrate adsorption on the active substance has a large influence on the reaction performance, which was elucidated by FT-IR characterization. Fig. 8A and C show that the adsorption peaks of CO weakened after 10 min until it disappeared. Both 13-Ni/ZrO$_2$ and 13-Ni$_3$P/ZrO$_2$ have a certain adsorption capacity for CO, but the adsorption strength is weak, which indicates that the activation of the active sites on the substrate is weak, so the conversion rate over ZrO$_2$ is relatively poor, and the ability of deep hydrogenation is not very strong. The reason for this may be related to the poor dispersion of the active site itself, on the one hand, and the poor interaction between the carrier and the active substance, on the other hand.

Fig. 8D and E show that 13-Ni/SiO$_2$ and 13-Ni$_3$P/SiO$_2$ have strong adsorption capacity for CO, indicating that both of them have strong activation ability for the substrate, and hence, the DEO conversion of both of them is greater than 99%. It is worth noting that the diversity of adsorption forms (linear, bridged adsorption) plays a critical role. When in the bridged adsorption mode, the DEO molecule connects *via* two sites. This makes it more difficult for the initial hydrogenation products to detach from the catalyst surface, and thus, facilitates deep hydrogenation. In contrast, linear adsorption inhibits deep hydrogenation by rapid detachment from the catalyst surface after initial hydrogenation is complete (Fig. 12). This might explain the large difference in product selectivity between the catalysts before and after phosphatization.

The 6,13,25-Ni$_3$P/SiO$_2$ catalyst showed a trend of decreasing Egly selectivity and high EG selectivity with an increase in nickel loading. Wu,[18] Ding[32] and Zhu[33] *et al.* suggested that
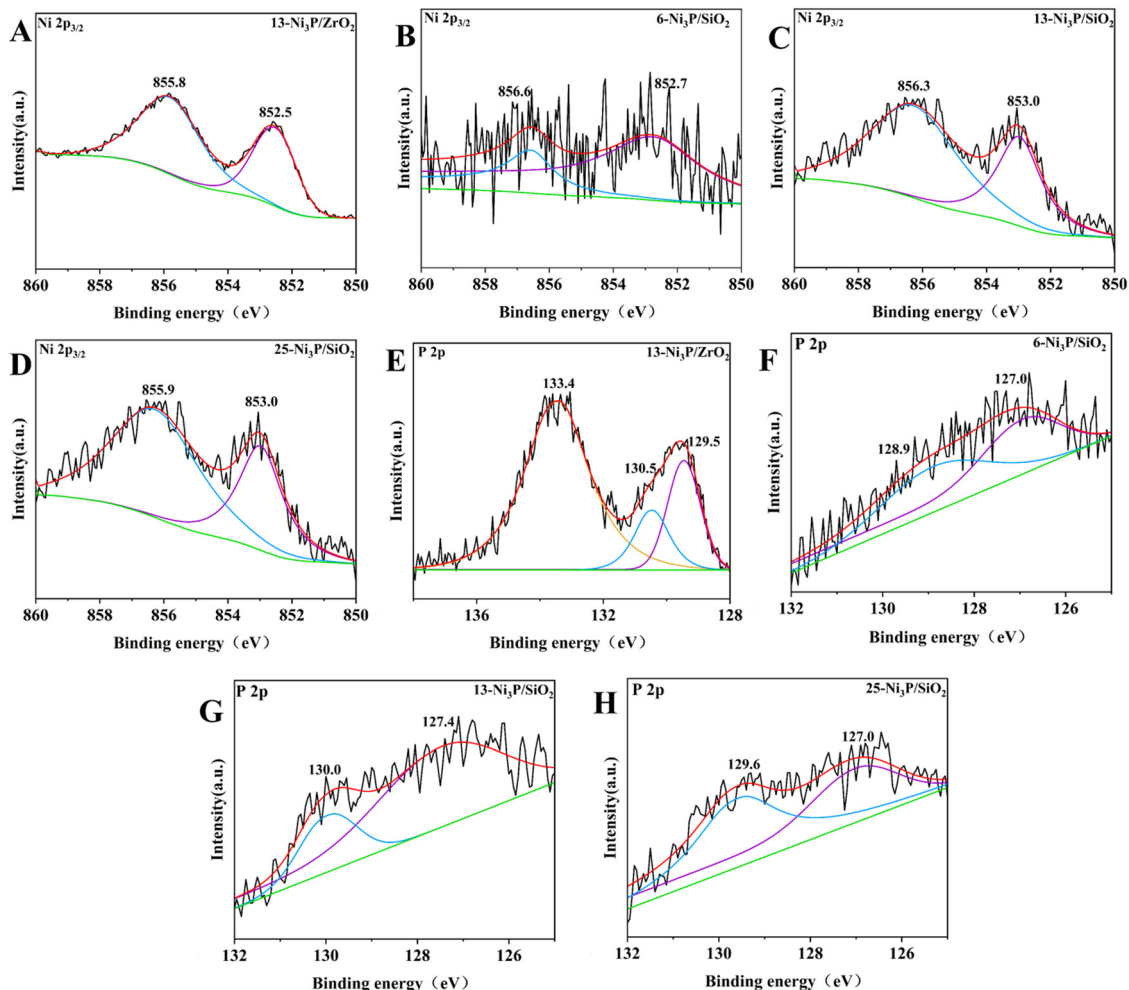
Fig. 10 . XPS spectra of passivated catalysts in the Ni 2p$_{3/2}$ and P 2p regions.

the surface acidic sites contribute to C=O/C–O bond breaking and selective hydrogenation. The NH$_3$-TPD (Fig. S6c–f, ESI†) results indicated that weak acidity and a relatively low acid content contribute to C=O/C–O bond activation. Therefore, the deep hydrogenation of Egly to EG and the dehydration between Egly and EtOH molecules are weak, and when the Ni content increases, both the surface acid strength and content increase in favor of C=O/C–O bond activation. As a result, the Egly selectivity decreases and the EG selectivity increases, which is in agreement with the evaluation results. The XRD results indicated the coexistence of Ni and Ni$_3$P crystalline phase with the increase in nickel loading, which indicated that there was a certain limit of the phosphatization effect when the Ni particle was relatively large. When the particles increase to a certain degree, the phenomenon of incomplete phosphatization occurs, and the TEM results also show that incomplete phosphatization leads to the phenomenon of decreasing dispersion and increasing particles. In addition, we believe that this result may lead to a gradual increase in the ratios of surface –Ni–Ni–Ni–Ni– and P–Ni–P–Ni–P with the increase in nickel loading, or the corresponding ratios of bridging/line adsorption gradually

increased. Ultimately, due to the increase in the ratio of bridging adsorption, the initial hydrogenation products are not easy to detach and are prone to go to deep hydrogenation.

5. Conclusion

In summary, the differences in the properties of 13-Ni/ZrO$_2$, 13-Ni$_3$P/ZrO$_2$, 13-Ni/SiO$_2$, and 13-Ni$_3$P/SiO$_2$ suggest that the introduction of phosphorus favors the segmentation of the Ni–Ni linkage; thus, it acts as a delimiter and exhibits segregation effect. The results of FT-IR and XRD evidenced that the existence of P transformed the surface metal distribution state from –Ni–Ni–Ni–Ni– to P–Ni–P–Ni–P. The former adsorbed CO as a combination of linear and bridging adsorption, while the latter was mainly dominated by linear adsorption. Bridging adsorption makes the preliminary hydrogenation products less likely to detach from the catalyst surface, thus facilitating deep hydrogenation, while linear adsorption inhibits deep hydrogenation *via* rapid detachment after the initial hydrogenation.
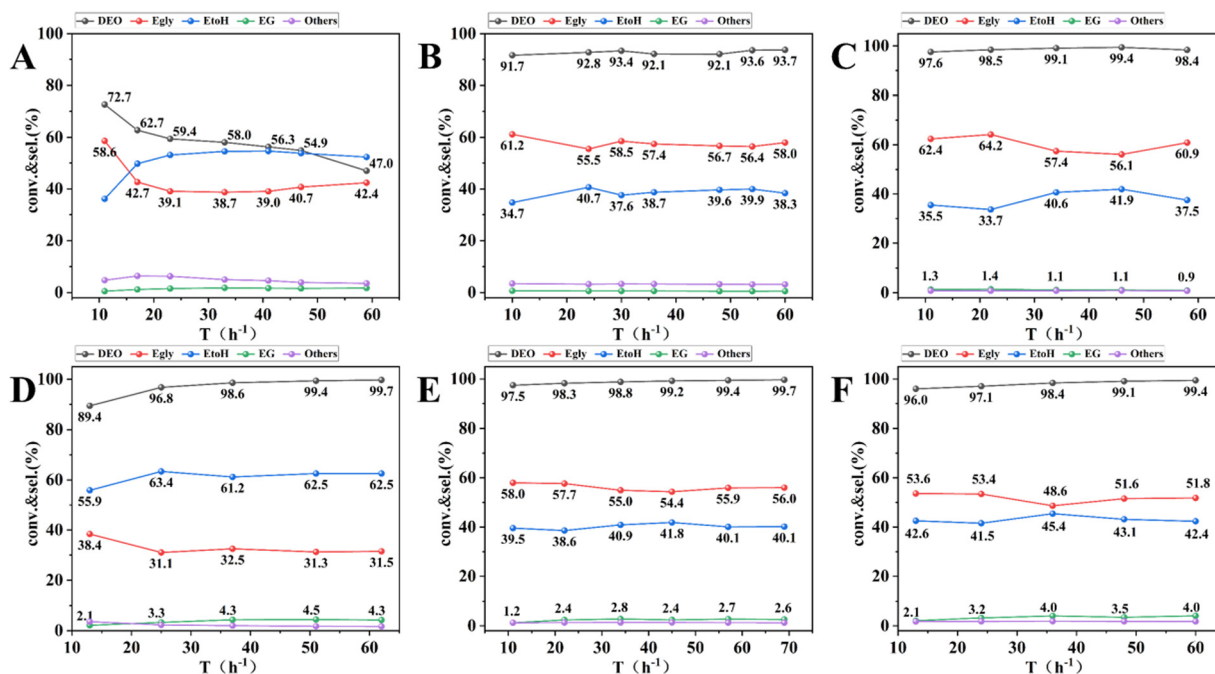
Fig. 11 Catalytic performance of synthesis catalysts. (A) 13-Ni/ZrO$_2$, (B) 13-Ni$_3$P/ZrO$_2$, (C) 6-Ni$_3$P/SiO$_2$, (D) 13-Ni/SiO$_2$, (E) 13-Ni$_3$P/SiO$_2$, and (F) 25-Ni$_3$P/SiO$_2$. Reaction conditions: P = 2.5 MPa, T = 220 °C, H$_2$/DEO molar ratio = 120, and WHSV = 0.5 h^{-1}. thers: ethyl ether, ethyl acetate, ethyl ethoxyacetate, 1,4-dioxane.
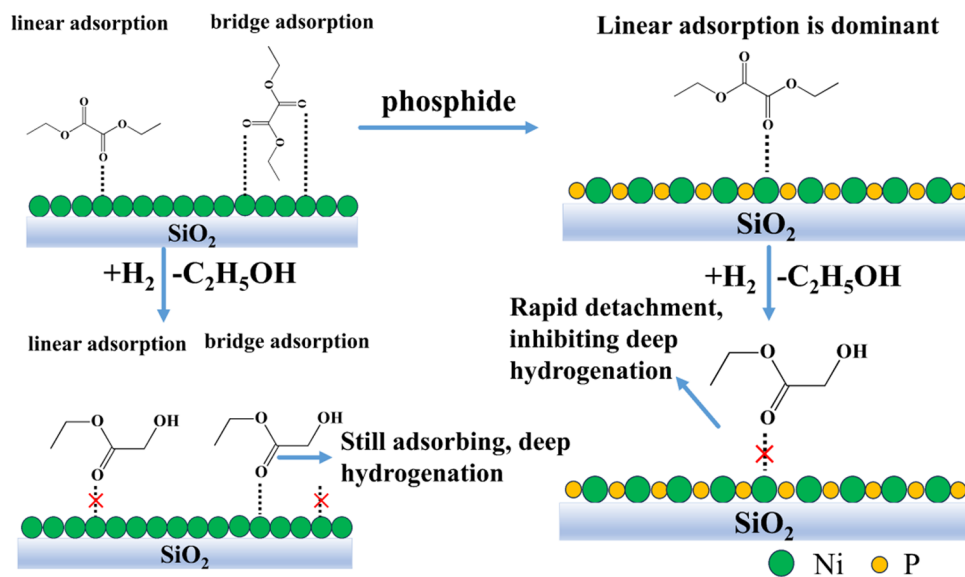

Fig. 12 Surface adsorption modeling of 13-Ni/SiO$_2$ and 13-Ni$_3$P/SiO$_2$.

The difference in the performance of the product selectivity of the 6,13,25-Ni$_3$P/SiO$_2$ catalysts shows that the incomplete phosphorylation with the increase in nickel loading gives rise to a state of coexistence of Ni and Ni$_3$P crystalline phases. This may lead to the coexistence of surface –Ni–Ni–Ni–Ni– and P–Ni–P–Ni–P and an increase in the corresponding bridging adsorption/linear adsorption ratios, making deep hydrogenation occur partially.

Conflicts of interest

There are no conflicts to declare.

Acknowledgements

References

1 B. W. Wang, Q. Xu, H. Song and G. H. Xu, *J. Nat. Gas Chem.*, 2007, **16**, 78–80.

2 Y. Sun, H. Wang, J. H. Shen, H. C. Liu and Z. M. Liu, *Catal. Commun.*, 2009, **10**, 678–681.

3 (*a*) G. F. Zhao, H. Li, J. Q. Si, Q. Nie, C. Meng, Y. Liu and Y. Lu, *ACS Sustainable Chem. Eng.*, 2021, **9**, 16719–16729; (*b*) P. K. Samantaray, A. Little, D. M. Haddleton, T. McNally, B. W. Tan, Z. Y. Sun, W. J. Huang, Y. Ji and C. Y. Wan, *Green Chem.*, 2020, **22**, 4055–4081.

4 (*a*) S. Y. Lee, J. C. Kim, J. S. Lee and Y. G. Kim, *Ind. Eng. Chem. Res.*, 1993, **32**, 253–259; (*b*) F. E. Celik, H. Lawrence and A. T. Bell, *J. Mol. Catal. A: Chem.*, 2008, **288**, 87–96.

5 Z. L. Zhuang, Y. H. Li, F. Chen, X. K. Chen, Z. Li, S. Y. Wang, X. P. Wang, H. J. Zhu, Y. Tan and Y. J. Ding, *Chem. Commun.*, 2022, **58**, 1958–1961.

6 (*a*) J. Zhu, L. Q. Cao, C. Y. Li, G. F. Zhao, T. Zhu, W. Hu, W. D. Sun and Y. Lu, *ACS Appl. Mater. Interfaces*, 2019, **11**, 37635–37643; (*b*) H. J. Huang, B. Wang, Y. Wang, Y. J. Zhao, S. P. Wang and X. B. Ma, *Catal. Today*, 2020, **358**, 68–73.

7 A. Y. Yin, C. Wen, W. L. Dai and K. N. Fan, *Appl. Catal., B*, 2011, **108**, 90–99.

8 H. M. Chen, J. J. Tan, J. L. Cui, X. H. Yang, H. Y. Zheng, Y. L. Zhu and Y. W. Li, *Mol. Catal.*, 2017, **433**, 346–353.

9 J. Sun, J. F. Yu, Q. X. Ma, F. Q. Meng, X. X. Wei, Y. N. Sun and N. Tsubaki, *Sci. Adv.*, 2018, 4.

10 B. Boardman, M. J. Hanton, H. van Rensburg and R. P. Tooze, *Chem. Commun.*, 2006, 2289–2291.

11 Y. Y. Cui, B. Wang, C. Wen, X. Chen and W. L. Dai, *ChemCatChem*, 2016, **8**, 527–531.

12 M. Abbas, Z. Chen and J. G. Chen, *J. Mater. Chem. A*, 2018, **6**, 19133–19142.

13 C. Wen, Y. Y. Cui, X. Chen, B. N. Zong and W. L. Dai, *Appl. Catal., B*, 2015, **162**, 483–493.

14 D. H. Wang, C. C. Zhang, M. Y. Zhu, F. Yu and B. Dai, *ChemistrySelect*, 2017, **2**, 4823–4829.

15 Y. N. Wang, X. P. Duan, J. W. Zheng, H. Q. Lin, Y. Z. Yuan, H. Ariga, S. Takakusagi and K. Asakura, *Catal. Sci. Technol.*, 2012, **2**, 1637–1639.

16 Y. F. Chen, L. P. Han, J. Zhu, P. J. Chen, S. Y. Fan, G. F. Zhao, Y. Liu and Y. Lu, *Catal. Commun.*, 2017, **96**, 58–62.

17 M. Abbas, J. Zhang, Z. Chen and J. G. Chen, *New J. Chem.*, 2018, **42**, 17553–17562.

18 P. Wu, J. Zhang, Z. J. Huang and J. A. Chen, *Fuel*, 2022, 324.

19 P. P. Bui, S. T. Oyama, A. Takagaki, B. P. Carrow and K. Nozaki, *ACS Catal.*, 2016, **6**, 4549–4558.

20 H. M. Chen, J. J. Tan, Y. L. Zhu and Y. W. Li, *Catal. Commun.*, 2016, **73**, 46–49.

21 (*a*) S. T. Oyama, X. Wang, Y. K. Lee, K. Bando and F. G. Requejo, *J. Catal.*, 2002, **210**, 207–217; (*b*) S. T. Oyama, X. Wang, Y. K. Lee and W. J. Chun, *J. Catal.*, 2004, **221**, 263–273.

22 (*a*) X. G. Liu, J. X. Chen and J. Y. Zhang, *Catal. Commun.*, 2007, **8**, 1905–1909; (*b*) X. G. Liu, J. X. Chen and J. Y. Zhang, *Ind. Eng. Chem. Res.*, 2008, **47**, 5362–5368.

23 S. F. Yang, C. H. Liang and R. Prins, *J. Catal.*, 2006, **237**, 118–130.

24 H. Zhang, R. Zhang, W. Zhang, B. Gu, Q. Tang, Q. Cao and W. Fang, *Appl. Catal., B*, 2023, 330.

25 H. Zhang, T. Y. Gao, Q. E. Cao and W. H. Fang, *ACS Sustainable Chem. Eng.*, 2021, **9**, 6056–6067.

26 (*a*) A. J. Wang, Z. Q. Yu, Y. Wang, G. Q. Zhang, Z. C. Sun, Y. Y. Liu, C. Shi and W. Wang, *J. Catal.*, 2022, **410**, 294–306; (*b*) S. Yang, G. B. Chen, A. G. Ricciardulli, P. P. Zhang, Z. Zhang, H. H. Shi, J. Ma, J. Zhang, P. W. M. Blom and X. L. Feng, *Angew. Chem., Int. Ed.*, 2020, **59**, 465–470; (*c*) G. X. Li, J. G. Wang, J. Y. Yu, H. Liu, Q. Cao, J. L. Du, L. L. Zhao, J. Jia, H. Liu and W. J. Zhou, *Appl. Catal., B*, 2020, 261; (*d*) Z. Q. Yu, K. B. Yao, Y. Wang, Y. L. Yao, Z. C. Sun, Y. Y. Liu, C. A. Shi, W. Wang and A. J. Wang, *Catal. Today*, 2021, **371**, 179–188.

27 Z. Q. Yu, Y. Wang, Z. C. Sun, X. Li, A. J. Wang, D. M. Camaioni and J. A. Lercher, *Green Chem.*, 2018, **20**, 609–619.

28 G. Huang, Z. C. Sun, Z. Q. Yu, Y. Y. Liu, Y. Wang, W. Wang, A. J. Wang and Y. K. Hu, *J. Catal.*, 2023, **419**, 37–48.

29 Z. Yu, Y. Yao, Y. Wang, Y. Li, Z. Sun, Y.-Y. Liu, C. Shi, J. Liu, W. Wang and A. Wang, *J. Catal.*, 2021, **403**, 194–202.

30 J. F. Li, Y. M. Chai, B. Liu, Y. L. Wu, X. H. Li, Z. Tang, Y. Q. Liu and C. G. Liu, *Appl. Catal., A*, 2014, **469**, 434–441.

31 J. A. Cecilia, A. Infantes-Molina, E. Rodriguez-Castellon, A. Jimenez-Lopez and S. T. Oyama, *Appl. Catal., B*, 2013, **136**, 140–149.

32 J. Ding, Y. Liu, J. Zhang, M. Dong, Y. Wang, W. He, Z. Lang, K. Liu and J. Chen, *Catal. Commun.*, 2017, **89**, 106–110.

33 Y. Zhu, X. Kong, X. Li, G. Ding, Y. Zhu and Y.-W. Li, *ACS Catal.*, 2014, **4**, 3612–3620.